Strong π-stacking causes unusually large anisotropic thermal expansion and thermochromism

Madushani Dharmarwardana[a,1], Brooke M. Otten[b,1], Mukunda M. Ghimire[b], Bhargav S. Arimilli[a], Christopher M. Williams[b], Stephen Boateng[b], Zhou Lu[b], Gregory T. McCandless[a], Jeremiah J. Gassensmith[a,2], and Mohammad A. Omary[b,2]

[a]Department of Chemistry and Biochemistry, University of Texas at Dallas, Richardson, TX 75080-3021; and [b]Department of Chemistry, University of North Texas, Denton, TX 76203

π-stacking in ground-state dimers/trimers/tetramers of *N*-butoxy-phenyl(naphthalene)diimide (BNDI) exceeds 50 kcal · mol^{-1} in strength, drastically surpassing that for the ^{*3}[pyrene]$_2$ excimer (~30 kcal · mol^{-1}; formal bond order = 1) and similar to other weak-to-moderate classical covalent bonds. Cooperative π-stacking in triclinic (BNDI-T) and monoclinic (BNDI-M) polymorphs effects unusually large linear thermal expansion coefficients (α_a, α_b, α_c, β) of (452, −16.8, −154, 273) × 10^{-6} · K^{-1} and (70.1, −44.7, 163, 177) × 10^{-6} · K^{-1}, respectively. BNDI-T exhibits highly reversible thermochromism over a 300-K range, manifest by color changes from orange (ambient temperature) toward red (cryogenic temperatures) or yellow (375 K), with repeated thermal cycling sustained for over at least 2 y.

π-stacking | naphthalene diimide | pyrene | anisotropic thermal expansion | thermochromism

Supramolecular π-stacking is an important phenomenon in multiple scientific disciplines; however, its strength is usually perceived (1) to be akin to van der Waals and multipole–multipole interactions (typically ≤5 kcal/mol) with no drastic effects on bulk optoelectronic or other material properties, such as band gap or thermal expansion. Here, we narrate another view of unusually strong π-stacking in metal-free organic molecules via several manifestations. First, we show that the π-stacking interactions can surpass conventional noncovalent interaction strength to attain weak-to-moderate classical covalent bond strength. Second, we show that cooperative π-stacking leads to unusually large thermal expansion, typically defined as "colossal" when manifest on the 10^{-4} · K^{-1} order of magnitude (2). Third, we show that purely π-stacking interactions can induce band-gap changes that cause otherwise colorless organic molecules to display drastic, reversible thermochromism in the solid state, among other previously unknown spectral and binding properties, even for classical chromophores.

It has been reported that so-called strong π-stacking interactions can be tuned to reach approximately 15 to 20 kcal · mol^{-1} by increasing the number of interacting electrons in polynuclear aromatic hydrocarbons such as pyrene (3) or coronene (1) dimers. An alternative strategy described herein, which leads to strong supramolecular interactions of ca. 50 kcal · mol^{-1}, is two-fold, emphasizing 1) reinforcing multipole–multipole interactions and 2) cooperativity in infinite solid-state stacking geometric motifs that preserves strong overlap between molecules. The reinforced cooperative π-stacking can then lead to the aforementioned bulk materials properties. Unusually large thermal expansion is rather rare yet quite desirable toward potential magneto-opto-electronic and gas storage applications (4–7). While examples of unusually large thermal expansion of inorganic (2, 8–10) and some organic salts (11) or metal-organic frameworks (MOFs) have become more common, examples involving metal-free organic semiconductors remain almost nonexistent (12). Polymeric (13–16) and liquid-crystalline systems (17–28) composed of n-type semiconducting (29, 30) naphthalene diimide (31,

32) and perylene analogs are known to exhibit temperature-dependent color changes (i.e., thermochromism) arising from intermolecular packing. Mechanistic description of packing changes has been made using optical spectroscopy and computational analysis with no temperature-dependent single-crystal studies done hitherto (33–35).

Here, we describe unusually strong π-stacking interactions in both a recently synthesized (BNDI) (36, 37) and a classical/prototypical organic π-stacking chromophore (pyrene), both experimentally and theoretically. Prior work on BNDI entailed physical changes to crystals upon heating, including thermosalient (36) and thermomorphic (37) behaviors with observational reference to thermochromic behavior (38) while referring to the present work herein as forthcoming to investigate the underlying mechanism in relation to π-stacking. Further, we report that two BNDI polymorphs not only show profound temperature-dependent structural changes but also unusually large thermal expansion rates on the same order of magnitude as those for inorganic systems. Additionally, the anisotropic expansion and underlying strong cooperative π-stacking induce a large change in the optical band gap in a metal-free single crystal to effect tunable/reversible multiple color changes. The π-stacking binding strength is compared to that in pyrene, whose ground-state dimer

---

Significance

π-stacking of polynuclear aromatic rings encompasses fundamental scientific phenomena in chemical bonding and photophysics with strong impacts on societal aspects that include electronic devices, DNA/RNA intercalation, and optical sensing of environmental pollutants. This work describes unusually strong π-stacking in a recently synthesized naphthalene-diimide derivative, as well as a prototypical π-stacked molecule, pyrene. The infinite/cooperative π-stacking in the former and dimer stacking in the latter are much stronger than previously thought to be possible for this type of supramolecular interaction, reaching ~50 and 20 kcal · mol^{-1}, respectively. This has led to unusually large anisotropic thermal expansion and multicycle/multicolor thermochromism in BNDI-T, whereas multiple unusual binding and photophysical properties have been discovered for the classical organic chromophore pyrene.

CHEMISTRY

is so strongly stacked that it causes physical discoloration of its crystalline solids and concentrated solutions versus the colorless dilute solutions, as well as a structured excimer emission profile upon direct excitation of dimer bands.

Results and Discussion

Structural Properties. BNDI (Fig. 1*A*) can be isolated in two polymorphs: a known (31) monoclinic polymorph (BNDI-M; Fig. 1*B*), as yellow needles (Fig. 1*C*), and a new triclinic system (BNDI-T; Fig. 1*D*), which forms red/orange rod-shaped crystals (Fig. 1*E*). See *SI Appendix* for bulk-synthesis details and selective preparation of either polymorph. Temperature-dependent single-crystal X-ray diffraction reveals that, across the temperature range studied, BNDI-T forms cofacial slipped-stacked sheets (Fig. 1*D*) versus a herringbone configuration for nonthermochromic BNDI-M (Fig. 1*C* and *SI Appendix*, Table S1 and Fig. S1), both with extended/infinite cooperative π-stacking of the NDI aromatic rings. The triclinic polymorph shows drastic negative thermochromism across a 275 K temperature range (Fig. 1 *F* and *G*). In contrast, BNDI-M demonstrates no variation in color at any of our tested temperatures. This is intriguing since the origin of the well-known thermochromic behavior found in polymeric (13–16) and liquid crystal samples (17–28) of NDI or perylene systems has never been adequately elucidated.

Anisotropic Thermal Expansion. Analysis of crystallographic data of both polymorphs shows unprecedented thermal expansion in unit cell sizes for these organic single crystals stemming from their cooperative π-stacking (Table 1). Single crystals of both BNDI-T and BNDI-M exhibit anisotropic thermal expansion behavior. The cell parameters are plotted versus temperature in *SI Appendix*, Figs. S2 and S3 for BNDI-T and BNDI-M, respectively, and are summarized in Tables 1 and 2. Data analyses show that BNDI-T and BNDI-M single crystals exhibit linear thermal expansion rates of $(\partial V/\partial T)_P = +0.191$ and $+0.247$ Å³ ·

K⁻¹, respectively, describing an overall anisotropic positive thermal expansion (PTE) upon cooling (*SI Appendix*, Figs. S2*D* and S3*D*). Upon cooling BNDI-T crystals from 375 to 90 K, the unit cell parameters b and c expand with respective rates of -1.36×10^{-4} and -3.06×10^{-3} Å · K⁻¹ (*SI Appendix*, Figs. S2*B* and S3*C*). This represents two orthogonal uniaxial negative thermal expansion (NTE) processes, whereas the a parameter contracts with a rate of $+2.01 \times 10^{-3}$ Å · K⁻¹—a uniaxial PTE. In contrast, BNDI-M shows a single uniaxial NTE expansion with a rate of -1.51×10^{-3} Å · K⁻¹ in only the unit cell parameter b, as illustrated in *SI Appendix*, Fig. S3*B*, whereas the a and c parameters contract with respective rates of $+3.52 \times 10^{-4}$ and $+1.63 \times 10^{-3}$ Å · K⁻¹ (*SI Appendix*, Fig. S3 *A* and *C*) over the same temperature range. These NTE/PTE parameters for BNDI-T and BNDI-M generally exceed literature values for inorganic and organometallic systems (Table 1). These purely organic (metal-free) solid-state systems, therefore, show unusually large thermal expansion behavior using the "colossal" standard defined by Goodwin et al. (2) for expansion/contraction rates surpassing 100×10^{-6} · K⁻¹ for individual $a/b/c$ parameters.

From a phenomenological standpoint, BNDI-T and BNDI-M manifest bona fide, pure NTE/PTE phenomena—as opposed to the gas adsorption–assisted/mediated NTE or PTE manifestation of the sort invoked in the literature for MOFs [e.g., MOF-5 (39) and FMOF-1 (2)] (i.e., the cause of the thermal expansion herein is cooperative π-stacking versus physisorption in these MOFs). The current observations are especially noteworthy given that the materials herein are nonporous without any detectable guest-accessible surface area (4, 7). We ascribe the unusually large thermal expansion in our materials to the flexibility of π-stacking "soft," dispersion-type interactions. Noble gas matrices like Xe (40) as well as ionic solids (2, 8, 10) are among prototypical materials that exhibit this phenomenon owing to similarly flexible dispersion interactions. The fact that the intermolecular π-stacking interactions occur as long-range interactions in
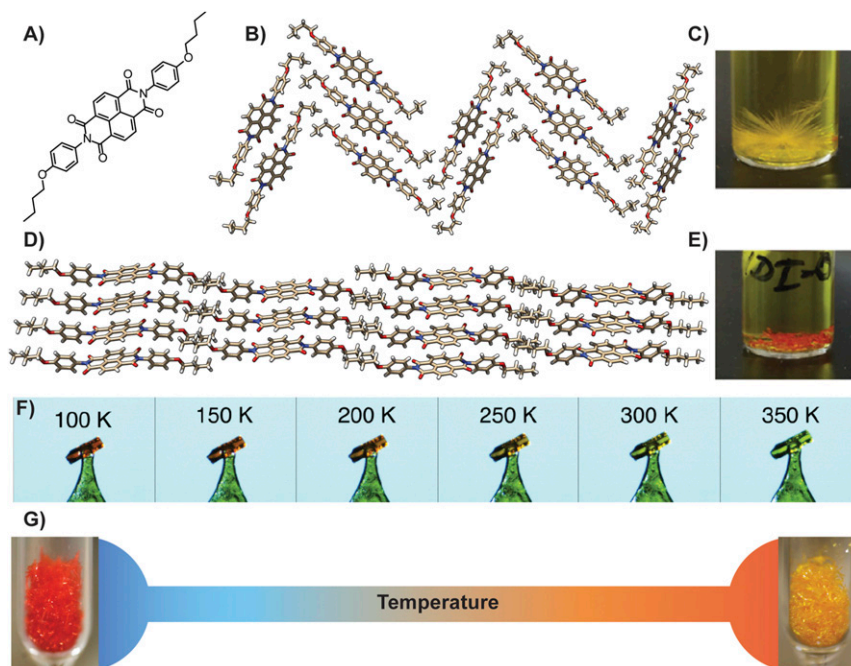
Fig. 1. (*A*) Molecular structure of BNDI. Two polymorphs of BNDI are shown. In both instances, BNDI molecules form infinite one-dimensional chains. (*B*) The herringbone arrayed monoclinic polymorph (BNDI-M) produces (*C*) yellow crystals while the (*D*) planar triclinic polymorph (BNDI-T) produces (*E*) red/orange crystals. (*F*) Images of a BNDI-T single crystal at different temperatures. The blue background behind the crystal causes yellow colors to appear greenish. (*G*) Photographs on the color scale illustrate reversible color change of BNDI-T upon cooling to ∼100 K and heating to 375 K. The color change is reversible for any number of cooling ↔ heating cycles (Movie S1).

Table 1. Anisotropic thermal expansion parameters for BNDI-T and BNDI-M versus literature precedents

Material	α_a/K^{-1}	α_b/K^{-1}	α_c/K^{-1}	β/K^{-1}	Reference
BNDI-T	4.52×10^{-4}	-1.68×10^{-5}	-1.54×10^{-4}	2.73×10^{-4}	This work
BNDI-M	7.01×10^{-5}	-4.47×10^{-5}	1.63×10^{-4}	1.77×10^{-4}	This work
IMACET	2.25×10^{-4}	2.38×10^{-4}	-2.90×10^{-4}		(60)
ZrW_2O_8	-9.10×10^{-6}	-9.10×10^{-6}	-9.10×10^{-6}	-2.70×10^{-5}	(8)
$Cd(CN)_2$	-2.00×10^{-6}	-2.00×10^{-6}	-2.00×10^{-6}		(10)
$AlPO_4$-17	-1.20×10^{-5}	-1.20×10^{-5}	-1.20×10^{-5}	-3.50×10^{-5}	(9)
$Ag_3[Co(CN)_6]$	1.50×10^{-4}	1.50×10^{-4}	-1.30×10^{-4}	1.60×10^{-4}	(2)
FMOF-1	2.30×10^{-4}	2.30×10^{-4}	-1.70×10^{-4}	3.00×10^{-4}	(4)
FMOF-1•N_2	-1.3×10^{-2}	-1.3×10^{-2}	1.20×10^{-2}	-1.0×10^{-2}	(4)
$Cu[PtBr_2(CN)_4]$	1.33×10^{-4}	-2.65×10^{-4}	4.36×10^{-4}		(61)
MOF-5	-1.60×10^{-5}	-1.60×10^{-5}	-1.60×10^{-5}		(39)

extended chains of organic NDI chromophores, as opposed to the simple, dimeric interactions in more conventional organic chromophores such as pyrene (41), should facilitate the manifestation of the phenomenon.

Thermochromism. Despite both polymorphs showing considerable solid-state dynamics and large changes in unit cell parameters upon cooling, a bathochromic shift in physical color is observed only in the BNDI-T polymorph. Qualitatively, the orange crystals of the triclinic polymorph gradually become dark red when the temperature is lowered to 100 K and then yellow upon heating to 375 K (Fig. 1). Moreover, this color change is reversible for many cycles of cooling and heating, and a long period over the course of at least 64 mo. From the analysis of crystallographic data, changes of molecular structure and packing could be quantified at both low and high temperatures (Fig. 2 and *SI Appendix*, Fig. S6). The most noticeable differences between the low- and high-temperature structures are illustrated in Fig. 2 *A* and *D* (42–44). In both systems, the interplanar distance (d_i; schematically illustrated in Fig. 2 *B* and *C*) changes similarly in both polymorphs by ∼0.1 Å over the tested temperature ranges, but only in the triclinic system do we observe an appreciable rotation of the appended butyl-phenoxy ring (Fig. 2*D*). At 100 K, the butoxyphenyl substituent rotation is 65.57(3)° versus 82.72(7)° at 375 K, approaching a perpendicular orientation relative to the plane of the NDI core. As a reference, the nonthermochromic BNDI-M has an average rotation of ∼80°, which only varies by ±1.4° between the 100 and 375 K structures (Table 2 and *SI Appendix*, Table S3). This rotation is tentatively attributed to the tighter packing arrangement in the low-temperature structure, which can be seen in the decreasing slippage distance and π–π overlap in the triclinic system.

The slippage distance (d_s) decreases considerably, by 0.76 Å, with the relative overlap of a pair of NDI cores increasing from

10 to 30%. When the planes of the NDI core are close together as such, the butoxyphenyl rings must twist to be less perpendicular than at higher temperatures in order to facilitate a closer packing arrangement. This phenomenon is reflected in significant changes of the unit cell parameters upon heating or cooling. Heating from 100 to 375 K results in an ∼8% increase in the unit cell volume because of cell expansion along the π–π stacking direction, which corresponds to the crystallographic *a*-axis stretching by approximately +13% (Table 2). Dihedral angle changes have a strong-yet-indirect impact upon the spectral bathochromic shift upon cooling BNDI-T. Smaller dihedrals lead to both shorter interplanar separations and stronger intermolecular π-overlap, as illustrated by Table 2 and Fig. 2; hence, there is a smaller energy gap between the highest occupied molecular orbital (HOMO) and lowest unoccupied molecular orbital (LUMO) for oligomers (or band gap for extended solids). The Table 2 and Fig. 2 data also illustrate that these correlations are insignificant or irrelevant for the BNDI-M chromophore, resulting in its lack of manifestation of thermochromism. Distinct from previous NDI and other polynuclear organic semiconductor investigations, the butoxy groups herein seem to allow triclinic polymorphs with stronger molecular overlap versus the common herringbone packing mode. We hypothesize that nBuO's oxygen atoms allow the albeit bulky nBu moieties to flex away from the π-chromophore moieties at the center of the molecule and allow them to overlap strongly. This is further borne out by the crystal structures in both this work and a literature precedent for a different organic semiconductor chromophore that attained strong extended chain overlap with nBuO but not cyclopentyl or nBu substituents (45).

These data suggest that greater π-overlap between NDI cores affects thermochromism in BNDI-T (46) in the solid-state structure. We were able to confirm if the change in the physical color of BNDI arises from oligomerization of BNDI

Table 2. Intramolecular and intermolecular structural parameters of BNDI-T and BNDI-M

T/K	a/Å	b/Å	c/Å	V/Å³	Dihedral angle/°	Interplanar distance/Å	CCDC number
BNDI-T							
100	4.1636(8)	8.1371(18)	20.104(5)	667.1(3)	65.57(3)	3.360	1497523
200	4.2634(10)	8.1305(11)	20.055(5)	680.6(2)	68.30(4)	3.401	1497522
298	4.4494(10)	8.1091(14)	19.887(4)	699.8(2)	73.82(5)	3.437	1497520
375	4.7207(18)	8.132(2)	19.200(6)	720.1(4)	82.72(7)	3.466	1497521
BNDI-M							
100	5.026(2)	33.756(5)	7.9533(14)	1,328.8(6)	79.30(4)	3.344	1497526
200	5.052(16)	33.718(9)	8.0290(2)	1,346.8(7)	79.68(6)	3.376	2067596
298	5.089(2)	33.584(14)	8.1530(4)	1,371.8(10)	79.97(5)	3.409	1497524
375	5.122(2)	33.298(14)	8.3320(4)	1,398.3(8)	80.75(7)	3.452	1497525
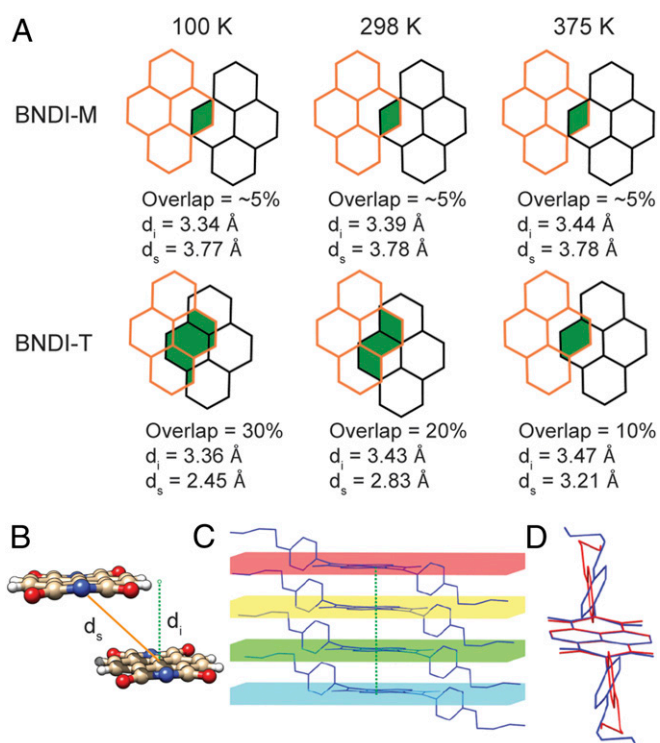
Fig. 2. π-slippage distances and percent π-overlapping between NDI cores: (*A*) Comparison between percent π-overlap, interplanar, and slipping distance for the two polymorphs at 100, 298, and 375 K. (*B*) Graphical illustration of distances measurements between an isolated dimer of BNDI. (*C*) The interplanar distance of BNDI-T is 3.360 Å at 100 K and increases to 3.466 Å at 375 K. (*D*) When planes are far apart, BNDI-T's phenyl rings are nearly perpendicular to the NDI plane (red structure), whereas when the planes are close together, the phenyl rings rotate (blue structure) to accommodate the decrease in free volume.

molecules in both the solid state and solution by ultraviolet-visible (UV-vis) electronic absorption spectroscopy. Temperature-dependent absorption studies of the thermochromic crystalline BNDI-T sample were also performed, revealing temperature-dependent band gap (E_g) values (Fig. 3 and *SI Appendix*, Table S2). These data are in excellent qualitative correlation with the reduction in the interplanar π-stacking distances and increased NDI ring overlap shown (Fig. 2*A*) in the temperature-dependent crystallographic data for this polymorph as well as the visual color changes of the solid crystalline BNDI-T material (Fig. 1 *F* and *G* and *SI Appendix*, Fig. S7). We are
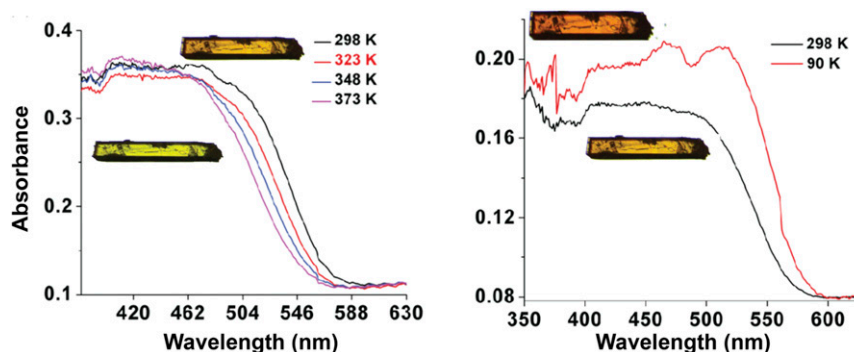
unaware of other organic n-type crystalline solids that show such a reversible thermal response, despite the discovery of semiconducting crystalline derivatives of NDI some 20 y ago (29). In contrast, the same spectral shifts and correlations thereof with the crystal structure or solid-state color variation with temperature do not exist for the BNDI-M polymorph (Fig. 3).

Solution Oligomerization. Fig. 4 shows polymorph- and concentration-dependent absorption spectra at room temperature for BNDI. At micromolar concentrations (Fig. 4*A*; trace f), the spectrum shows the typical discrete absorption lines corresponding to vibronically-resolved π–π* electronic transitions within BNDI monomers (*SI Appendix*, Fig. S15). Notably, there is an abrupt loss of optical absorption at 400 nm. If the BNDI molecules did not interact with each other in solution, one would expect to see only an increase in absorbance at higher concentrations. However, a bathochromic shift of the cutoff wavelengths at higher concentrations in solution is clearly observed. In Fig. 4*B*, the absorption spectra of solutions of BNDI molecules in chloroform at ambient temperature are shown in the concentration range of 0.1 to 1.0 mM. The large bathochromic shift is a reflection of oligomerization taking place as concentration increases (47). From the concentration-dependent studies for the data set shown in Fig. 4*C*, the extinction coefficient, formation constant, and free energy were quantified as 1,130 $M^{-1} \cdot cm^{-1}$, $1.25 \times 10^{19} \cdot M^{-3}$, and −26.1 kcal $\cdot$ mol^{-1}, respectively, for a $[BNDI]_4$ tetramer in chloroform solution. The fitting model followed that described by the Adamson (48) and the Patterson (47) groups for cyano complexes. The $[BNDI]_4$ tetramer likely exists in equilibria with monomer, dimer, trimer, and other possible $[BNDI]_n$ oligomers, as found in one precedent publication (47), which complicates the quantitative analysis for the thermodynamic parameters of each oligomer. However, the qualitative trend is unmistakable for the red shifting of absorption cutoff at higher concentrations based upon the data in Fig. 4*A*.

Comparison with Pyrene Dimerization as a "Control." We repeated the experiment with pyrene, which provides a "control" for the cooperative π-stacking in BNDI-T, as pyrene solids π-stack as mere dimers as opposed to infinite chains. In addition, the pyrene excimer (excited dimer) is also used as the yardstick for strong intermolecular interactions in aromatic π-stacked systems with a formal-bond-order of 1; we recognize, however, a legitimate alternative view that covalency should not be used to describe such excimeric bonding, reserving it to classical bonds between a mere two atoms. The visible absorption peaks of pyrene appear with a surprisingly high resolution at ca. 410, 425, and 450 nm in both the crystalline solid state and solution in the 0.01 to 0.1 M range in cyclohexane. Analysis of the concentration-dependent UV-vis data in Fig. 4 *E* and *F* gives rise
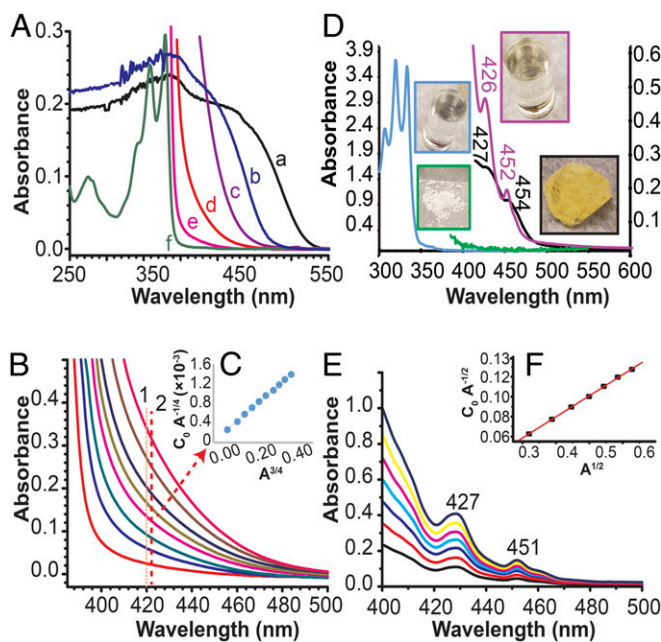

Fig. 3. Comparison of solid-state absorption spectra for BNDI-T crystals versus temperature, showing the (*Left*) hypsochromic shifts when heated from room temperature to higher temperature and (*Right*) bathochromic shifts when cooled from room temperature to cryogenic temperatures.

Fig. 4. (*A*) Solid-state versus concentration-dependent solution UV-vis spectra of BNDI-T at ambient temperature. Spectra labeled *a* and *b* are diffuse reflectance spectra for solid samples of BNDI-T and BNDI-M, respectively, whereas spectra *c* to *f* are for 1.0 mM, 0.1 mM, 0.01 mM, and 1.0 μM solutions, respectively, in chloroform. A bathochromic shift occurs with increasing BNDI concentration approaching the solid-state absorption cutoff for BNDI-T. (*B*) Absorption spectra versus concentration of 0.1 to 1 mM BNDI-T chloroform solutions at ambient temperature in a 1-cm cell. (*C*) A plot of $c_0A^{-1/4}$ versus $A^{3/4}$ with absorbance values taken at feature two to represent BNDI monomer-to-tetramer equilibrium. (*D*) UV-vis spectra of pyrene in 0.1 M solution in cyclohexane or the crystalline solid state showing visible dimer absorption peaks that bleach upon disruption of crystallinity by grinding. (*E*) UV-vis spectra of pyrene solutions versus concentration in cyclohexane in a 10-cm cell. (*F*) A plot of $c_0A^{-1/2}$ versus $A^{1/2}$ with absorbance values taken at the visible band maxima from (*E*) data to represent pyrene monomer-to-dimer equilibrium.

to an extinction coefficient, formation constant, and free energy of 0.946 $M^{-1} \cdot cm^{-1}$, 4,530 M^{-1}, and −4.99 kcal · mol^{-1}, respectively, for the [pyrene]$_2$ dimer. The better fitting of BNDI data to a tetramer in contrast to dimer for pyrene in solution is consistent with the infinite-stack versus dimer packing, respectively, and the experimental free energies of both the pyrene and NDI systems are in reasonable agreement with density functional theory (DFT)-computed values (vide infra).

The pyrene solid, on the other hand, can be excited directly at the visible dimer absorption peaks discovered herein, leading to the static excimer band as opposed to the well-known dynamic excimer band. The former emission is vibronically structured, which corresponds to intermolecular vibrations that are further validated by experimental/computational infrared (IR) spectra (Movie S2). This defies the conventional picture that the dimer dissociates before it can complete a vibrational cycle, owing to too few pyrene molecules being at close enough distance for significant excitation of the ground-state pairs to the excimer to occur, thus normally leading to unstructured emission. The static excimer emission is also associated with the annihilation of the risetime component in the time-resolved spectra (*SI Appendix*, Fig. S8), because the mechanism does not require collision of an excited monomer with a ground-state monomer that leads to risetime in dynamic excimers. These results for pyrene solid luminescence narrate another view about the photophysics of this classical compound—besides the aforementioned finding about its visible absorption bands in the crystalline solid state, as

anticipated in the foremost review on preassociated pyrenes by Winnik (49). While BNDI-T was not luminescent even at cryogenic temperatures, we managed to record similar solid-state IR data that underscore multiple intermolecular vibrations correlated with DFT-computed spectra (Movie S3).
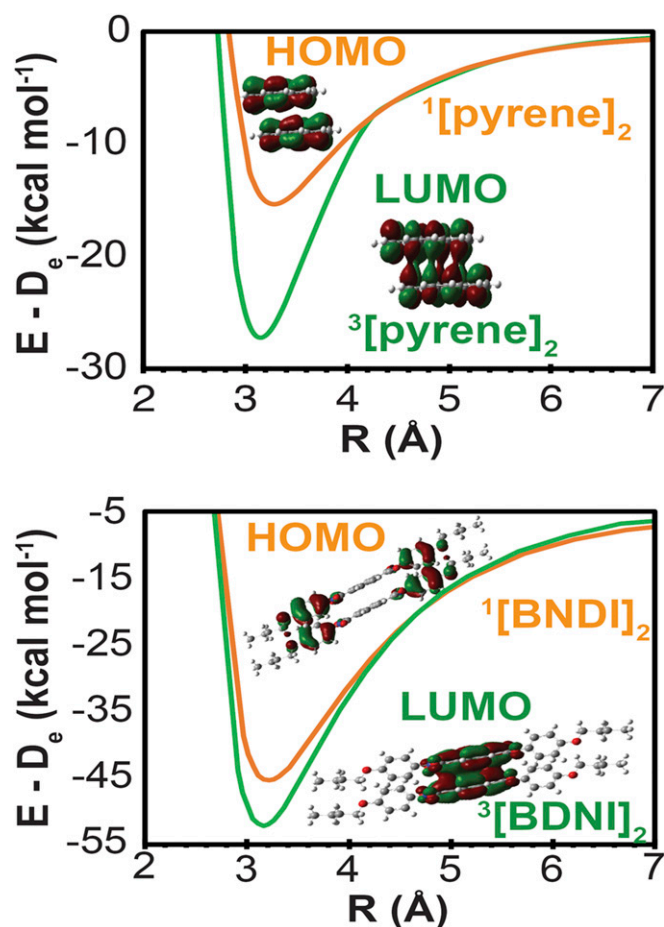
The optical changes in BNDI upon polymorphism, the thermochromism changes within the BNDI-T polymorph, the solution changes upon increasing the concentration of either BNDI polymorph or pyrene, and the discoloration of pyrene in the solid-state or concentrated solutions are all related to stronger π-stacking that leads to red-shifted absorption bands. Stronger binding, which is manifest by shorter π-stacked intermolecular distances as well as a greater extent of molecular overlap, further leads to a smaller band gap for the solid or HOMO–LUMO gap for an oligomer. Thus, as such optical energy gaps become smaller upon going from BNDI-M to BNDI-T, or as the latter goes from higher to lower temperatures, the absorption band undergoes a red shift that results in a more reddish color for BNDI-T compared to BNDI-M or thermochromism for BNDI-T from more yellowish colors at higher temperatures to more reddish colors at cryogenic temperatures. Likewise, correlations take place as either BNDI or pyrene increases solution concentration or as pyrene discolors yellow in the solid states or at highly-concentrated solutions with respect to the colorless dilute solutions.

Supportive Theory. The results of DFT and time-dependent DFT (TD-DFT) calculations related to the aforementioned experimental phenomena are included in Table 3, Fig. 5, and *SI Appendix*, Figs. S10–S17 and Tables S3–S15. The NDI monomer shows ambipolar character, as evident in molecular electrostatic potential maps (*SI Appendix*, Fig. S13), which illustrate greater charge separation and greater magnitude of quadrupole moments in BNDI than pyrene. These results suggest major electrostatic contributions to the stacking mode of BNDI solids, more so than in pyrene. Thus, such electrostatic forces assist in

Table 3. Supramolecular bond energies (ΔE/bond in kcal/mol) and equilibrium distances between monomer ring-planes (R_e in Å) in [BNDI]$_2$, [BNDI]$_3$, and [pyrene]$_2$ in both the ground and excited states (S_0 and T_1, respectively)

[BNDI]$_2$		ΔE_1/bond	ΔE_2/bond	R_e
BNDI-T: B97D/CEP-121G(d)		−41	N/A	3.47
BNDI-M: B97D/CEP-121G(d)		−33	N/A	3.41
B97D/CEP-121G(d)	Ground state	−42	−44	3.21
	Excited state	−52	−52	3.16
B97D/CEP-31G(d)	Ground state	−50	−54	3.19
	Excited state	−61	−66	3.12
B97D/6-31G*	Ground state	−47	−51	3.26
	Excited state	−56	−64	3.16
[BNDI]$_3$				
B97D/CEP-121G(d)	Ground state	−43	−46	3.19
B97D/CEP-31G(d)	Ground state	−51	−56	2.98
[BNDI]$_4$				
B97D/CEP-31G(d)	Ground state	−52	−57	3.14
[Pyrene]$_2$				
B97D/CEP-121G(d)	Ground state	−15	−15	3.28
	Excited state	−24	−27	3.15
B97D/CEP-31G(d)	Ground state	−19	−20	3.21
	Excited state	−29	−32	3.12

The "BNDI-T" and "BNDI-M" entries are from single-point calculations for the [BNDI]$_2$ dimer models at their respective crystallographic geometry at 298 K; remaining results are from structure optimizations (full optimization for ΔE_1/bond and PES for ΔE_2/bond).

Dharmarwardana et al.
Strong π-stacking causes unusually large anisotropic thermal expansion and thermochromism

Fig. 5. One-dimensional PES plots for [pyrene]$_2$ (*Top*) and [BNDI]$_2$ (*Bottom*) in their respective S$_0$ ground state (orange) and T$_1$ lowest-triplet excited state (green); HOMO (top/S$_0$ insets) and LUMO (bottom/T$_1$ insets) contours are also shown in PES plots.

governing the extended structure of BNDI-T and BNDI-M solids (and even in solution to tetramers for either BNDI solid, as opposed to mere dimers in both the solid state and nearly saturated solutions of pyrene).

Binding energies for the pyrene dimer in the singlet ground state, determined through complete optimization of [pyrene]$_2$ and the pyrene monomer, attain 15.0 kcal · mol^{-1} using B97D/CEP-121G(d), similar to Grimme's 13.0 kcal · mol^{-1} in the reported literature (3). When this molecule is excited, an increase of the binding energy to 24.1 kcal · mol^{-1} is attained, as expected given the electronic transition from a π*-antibonding HOMO to a π-bonding LUMO (Fig. 5, *Top*), hence increasing the formal bond order from 0/ground-state dimer to 1/excited-state excimer. Altering the basis set to CEP-31G(d) increases the pyrene dimer and excimer binding energies to 19.5 and 29.1 kcal/mol, respectively. This phenomenon is also seen, albeit to a lesser extent, for [BNDI]$_2$, where the calculated binding energy in the ground state is 41.6 (49.7) kcal · mol^{-1} and upon excitation this increases to 52.2 (61.3) kcal · mol^{-1} using B97D/CEP-121G(d) [Fig. 5, *Bottom*; or B97D/CEP-31G(d) for the parenthesized values]. These findings underscore the major theme of this work that π-stacking in ground-state BNDI dimers/oligomers nearing/exceeding ∼50 kcal · mol^{-1}, drastically surpassing the binding energy of the *^{3}[pyrene]$_2$ excimer (formal bond order = 1) by ∼20 kcal · mol^{-1}. Using a more conventional Pople's basis set, 6-31G*, attains BNDI dimer and excimer binding energies of 46.6 and 56.4 kcal · mol^{-1}, respectively, which is rather similar to

B97D/CEP-31G(d) results. Other literature systems that exhibited extended π-stacking with oligomeric association in solution include those described by Chan and Yam for Pt(II)-alkynyl/polypyridines; however, despite the assistance by Pt(II)–Pt(II) interactions, the association energy remains at ∼6 kcal · mol^{-1}, well short of values obtained experimentally and computationally in this work by approximately one order of magnitude (50). Higher association energies of ∼18 kcal · mol^{-1} were obtained for such complexes in organogel media, but the gelation energy was the main contribution, and the values remain almost three times lower than those in this work (51). Lastly, for literature comparisons, an investigation by Grimme of π-stacking of acene (from n = 1 = benzene to n = 4 = tetracene) dimers at different association modes reveals association energies of 2.5 to 18.9 kcal · mol^{-1} (52) (i.e., with the highest values in the neighborhood of the aforementioned value for the pyrene dimer by the same author). The experimental ΔG (298 K) is ∼26 kcal · mol^{-1} based on Fig. 4 UV-vis data analysis (vide supra) compared to theoretically-obtained 22 to 28 kcal · mol^{-1} (*SI Appendix*, Tables S4 and S15 for gas phase and solution, respectively) and manifesting excellent agreement.

Orbital analysis upon [BNDI]$_2$ reveals lesser orbital delocalization and less clear π*$_{HOMO}$→π$_{LUMO}$ assignment (Fig. 5, *Bottom*) and hence lesser stabilization in the excimeric state. The increase in the binding energy in BNDI versus pyrene dimerization is a result of the combination of π-molecular overlap and multipole–multipole electrostatic interactions, as established for the latter from the MEP/ESP analysis discussed previously. The higher binding energies seen for the BNDI system are also seen for the crystal structures of the BNDI-T/BNDI-M polymorphs (Table 3 and *SI Appendix*, Table S5). Rigid one-dimensional potential-energy surfaces (PES) for both the pyrene and BNDI systems are shown in Fig. 5. Another noteworthy finding is that the ground-state attraction in [pyrene]$_2$ is much more significant than what is usually dismissed as a dissociated pyrene dimer without a potential-well minimum in PES illustrations in typical organic chemistry textbooks and review articles on pyrene photophysics, which typically illustrate a potential-well minimum only for the *[pyrene]$_2$ excimer (49, 53). We believe that dispersion interactions—both π-stacking and multipole–multipole types—are unusually strong in both pyrene and BNDI dimers because they involve a large number of interacting electrons (1, 3, 54, 55). Such interactions are, we hypothesize, responsible for the colors exhibited by solids and concentrated solutions of both organic compounds. Indeed, for BNDI, the DFT calculations suggesting higher cohesive energies for trimer and tetramer models (Table 3 and *SI Appendix*, Table S4) may be extrapolated to the infinite-chain model of the solid to explain its thermochromism in the visible region. Thus, even the 52.0 (−ΔE$_1$/binding) and 57.0 kcal/mol (ΔE$_2$/binding) supramolecular interaction energy computed for the ground-state BNDI tetramer using B97D/CEP-31G(d) represents a lower limit for the binding in this solid. The trend of ∼1.5 to 2.0 kcal/mol greater stabilization per supramolecular interaction in tetramer versus trimer versus dimer models of BNDI are also consistent with the experimental ΔG for a tetramer (Fig. 4C versus Table 3 and *SI Appendix*, Table S4). Additional stabilization beyond a tetramer is anticipated in the solid state, especially for the BNDI-T polymorph that exhibits greater π-overlap (Fig. 2) and stronger binding (Table 3 and *SI Appendix*, Table S5) versus BNDI-M.

Cooling BNDI-T increases the attractive energy between adjacent BNDI units, allowing them to be closer to the potential minimum in the pertinent ground-state PES, which leads to a red-shifted absorption, whereas heating leads to the opposite effects. For the nonthermochromic BNDI-M polymorph, the calculated lowest-energy absorption band does not shift appreciably (*SI Appendix*, Figs. S14, *i* and S17, *a*); however, applying the same theoretical treatment for BNDI-T reveals a

significant red-shifted absorption upon cooling, corresponding to the thermochromic shift seen experimentally (*SI Appendix*, Figs. S14, *ii* and S17, *b*). This change in λ_{max} is attributed to the change in the percent overlap of the naphthalene rings as well as R_e, as shown in the *SI Appendix*, Fig. S11. The overall thermochromic shifting of the bands is 10 times larger for the BNDI-T polymorph (1,166 cm^{-1}) than seen for the BNDI-M polymorph (117 cm^{-1}). The supramolecular interaction being long-range and anisotropic in BNDI solids is consistent with the anisotropic PTE/NTE. The supramolecular interactions contract upon cooling along the stacking axis, whereas expansion occurs in other crystallographic directions. Pyrene, on the other hand, exhibits supramolecular π-stacking only within localized dimer units as opposed to long-range stacking; as a result, neither thermochromism nor significant anisotropic NTE/PTE takes place for pyrene. Nevertheless, the strong π-stacking—even being restricted to the dimer level—attains remarkable photophysical phenomena that challenge myths about this classic molecule. TD-DFT data also qualitatively reproduce experimental UV-vis data versus concentration, showing red-shifted absorption bands upon oligomerization in chloroform or gas phase (*SI Appendix*, Fig. S16 or S14, respectively; *SI Appendix*, Tables S11 and S12). Although both BNDI-M and BNDI-T polymorphs pack in a head-to-head mode, the overlapping areas and change thereof versus temperature influence the spin-allowed excited states. The intramolecular charge transfer (from phenoxy groups to the central NDI region) states dim in larger overlapping BNDI-T polymorphs and localized excited states dominate the electronic transitions upon aggregation (*SI Appendix*, Tables S13 and S14).

Conclusions and Prospects

Certain aromatic systems are shown to exhibit cooperative π-stacking/multipole–multipole interactions of great strength, akin to those in weak-to-moderate classical covalent bonds, leading to attainment of large anisotropic thermal expansion and reversible thermochromism. One of these, BNDI, shows perhaps the largest effects known in a metal-free/nonporous organic crystalline material. We also describe phenomena for pyrene at odds with accepted knowledge of this classic chromophore, including significant/nonvanishing ground-state π-stacking interactions that cause solid-state/solution discoloration and structured excimer emission upon direct-dimer excitation. Besides the drastic thermochromic and anisotropic thermal expansion changes herein, the consequences of these findings are expected to have significant roles in other technological/biochemical areas including RNA/DNA intercalation (56, 57), rigidochromic/environmental sensing (58, 59), etc.

Materials and Methods

Crystallography: A Bruker Kappa D8 Quest diffractometer was equipped with an Incoatec microfocus Mo Kα radiation source, HELIOS multilayer optics, Oxford Cryosystems cryostream, and a Photon 100 CMOS detector. UV-vis: Transmission (solutions or thin films/double-beam) and diffuse reflectance (powders or crystals/single beam via an integrating sphere) were measured using a Perkin–Elmer Lambda 900 spectrophotometer. Photoluminescence: A PTI Quanta Master Model QM-4 scanning spectrofluorometer was used. DFT calculations: Grimme's GGA-type density B97D and Truhlar's M06 functionals together with CEP-31G(d), CEP-121G(d), and 6-31G* basis sets were used. TD-DFT spectra: CAM-B3LYP functional with Grimme's D3-BJ damping dispersion corrections with Pople's 6-31G** basis sets were used. Vibronically resolved spectra: CIS/6-31G** was used.

Representative Synthetic Procedure of BNDI-T. As-synthesized BNDI solid (0.056 g, 1.0 mmol) and tetrabutylammonium bromide (2.0 mmol) were placed in a vial and dissolved with 2.0 mL of CHCl$_3$ and boiled until the solid particles disappeared. The resultant solution was used for single-crystal growth by slow evaporation to attain orange crystals (0.040 g; 71% yield).

Data Availability. All study data are included in the article and/or supporting information.

1. Y. Zhao, D. G. Truhlar, A prototype for graphene material simulation: Structures and interaction potentials of coronene dimers. *J. Phys. Chem. C* **112**, 4061–4067 (2008).
2. A. L. Goodwin *et al.*, Colossal positive and negative thermal expansion in the framework material Ag3[Co(CN)6]. *Science* **319**, 794–797 (2008).
3. S. Grimme, Semiempirical GGA-type density functional constructed with a long-range dispersion correction. *J. Comput. Chem.* **27**, 1787–1799 (2006).
4. C. Yang, X. Wang, M. A. Omary, Crystallographic observation of dynamic gas adsorption sites and thermal expansion in a breathable fluorous metal-organic framework. *Angew. Chem. Int. Ed. Engl.* **48**, 2500–2505 (2009).
5. D. Dubbeldam, K. S. Walton, D. E. Ellis, R. Q. Snurr, Exceptional negative thermal expansion in isoreticular metal-organic frameworks. *Angew. Chem. Int. Ed. Engl.* **46**, 4496–4499 (2007).
6. S. S. Han, W. A. Goddard, Metal–organic frameworks provide large negative thermal expansion behavior. *J. Phys. Chem. C* **111**, 15185–15191 (2007).
7. J. L. Rowsell, E. C. Spencer, J. Eckert, J. A. Howard, O. M. Yaghi, Gas adsorption sites in a large-pore metal-organic framework. *Science* **309**, 1350–1354 (2005).
8. T. A. Mary, J. S. O. Evans, T. Vogt, A. W. Sleight, Negative thermal expansion from 0.3 to 1050 kelvin in ZrW$_2$O$_8$. *Science* **272**, 90–92 (1996).
9. M. P. Attfield, A. W. Sleight, Exceptional negative thermal expansion in AlPO4-17. *Chem. Mater.* **10**, 2013–2019 (1998).
10. A. L. Goodwin, C. J. Kepert, Negative thermal expansion and low-frequency modes in cyanide-bridged framework materials. *Phys. Rev. B* **71**, 140301 (2005).
11. I. de Pedro *et al.*, On the colossal and highly anisotropic thermal expansion exhibited by imidazolium salts. *Cryst. Growth Des.* **15**, 5207–5212 (2015).
12. T. He *et al.*, Single-crystal field-effect transistors of new Cl$_2$-NDI polymorph processed by sublimation in air. *Nat. Commun.* **6**, 5954–5963 (2015).
13. M. Carlotti *et al.*, Thermochromic polyethylene films doped with perylene chromophores: Experimental evidence and methods for characterization of their phase behaviour. *Polym. Chem.* **6**, 4003–4012 (2015).
14. A. Seeboth, D. Lötzsch, R. Ruhmann, O. Muehling, Thermochromic polymers—Function by design. *Chem. Rev.* **114**, 3037–3068 (2014).
15. A. Bohm, M. Krieger, S. Becker, K. Mullen, "Thermochromic rylene dyes." US patent 6486319B1 (2002).
16. S. Becker, A. Böhm, K. Müllen, New thermotropic dyes based on amino-substituted perylenedicarboximides. *Chemistry* **6**, 3984–3990 (2000).
17. Z. Chen *et al.*, Photoluminescence and conductivity of self-assembled pi-pi stacks of perylene bisimide dyes. *Chemistry* **13**, 436–449 (2007).
18. J. van Herrikhuyzen, A. Syamakumari, A. P. Schenning, E. W. Meijer, Synthesis of n-type perylene bisimide derivatives and their orthogonal self-assembly with p-type oligo(p-phenylene vinylene)s. *J. Am. Chem. Soc.* **126**, 10021–10027 (2004).
19. V. Percec *et al.*, Transformation from kinetically into thermodynamically controlled self-organization of complex helical columns with 3D periodicity assembled from dendronized perylene bisimides. *J. Am. Chem. Soc.* **135**, 4129–4148 (2013).
20. I. K. Iverson, S. M. Casey, W. Seo, S.-W. Tam-Chang, B. A. Pindzola, Controlling molecular orientation in solid films via self-organization in the liquid-crystalline phase. *Langmuir* **18**, 3510–3516 (2002).
21. F. Würthner, C. Thalacker, S. Diele, C. Tschierske, Fluorescent J-type aggregates and thermotropic columnar mesophases of perylene bisimide dyes. *Chemistry* **7**, 2245–2253 (2001).
22. B. A. Gregg, R. A. Cormier, Liquid crystal perylene diimide films characterized by electrochemical, spectroelectrochemical, and conductivity versus potential measurements. *J. Phys. Chem. B* **102**, 9952–9957 (1998).
23. R. A. Cormier, B. A. Gregg, Self-organization in thin films of liquid crystalline perylene diimides. *J. Phys. Chem. B* **101**, 11004–11006 (1997).
24. B. A. Gregg, R. A. Cormier, Doping molecular semiconductors: n-type doping of a liquid crystal perylene diimide. *J. Am. Chem. Soc.* **123**, 7959–7960 (2001).
25. F. Würthner *et al.*, Perylene bisimide dye assemblies as archetype functional supramolecular materials. *Chem. Rev.* **116**, 962–1052 (2016).
26. M. Gsänger *et al.*, A crystal-engineered hydrogen-bonded octachloroperylene diimide with a twisted core: An n-channel organic semiconductor. *Angew. Chem. Int. Ed. Engl.* **49**, 740–743 (2010).
27. L. Schmidt-Mende *et al.*, Self-organized discotic liquid crystals for high-efficiency organic photovoltaics. *Science* **293**, 1119–1122 (2001).
28. F. Würthner, Z. Chen, V. Dehm, V. Stepanenko, One-dimensional luminescent nanoaggregates of perylene bisimides. *Chem. Commun.* **37**, 1188–1190 (2006).

Dharmarwardana et al.
Strong π-stacking causes unusually large anisotropic thermal expansion and thermochromism

PNAS | 7 of 8
https://doi.org/10.1073/pnas.2106572118

CHEMISTRY

29. H. E. Katz *et al*., A soluble and air-stable organic semiconductor with high electron mobility. *Nature* **404**, 478–481 (2000).

30. X. Zhan *et al*., Rylene and related diimides for organic electronics. *Adv. Mater.* **23**, 268–284 (2011).

31. R. Rybakiewicz *et al*., New semiconducting naphthalene bisimides N-substituted with alkoxyphenyl groups: Spectroscopic, electrochemical, structural and electrical properties. *Rsc Adv* **4**, 14089–14100 (2014).

32. M. A. Kobaisi, S. V. Bhosale, K. Latham, A. M. Raynor, S. V. Bhosale, Functional naphthalene diimides: Synthesis, properties, and applications. *Chem. Rev.* **116**, 11685–11796 (2016).

33. T. D. Bell *et al*., Melt-induced fluorescent signature in a simple naphthalenediimide. *Chem. Commun.* **46**, 4881–4883 (2010).

34. N. Mizoshita, T. Tani, S. Inagaki, Isothermally reversible fluorescence switching of a mechanochromic perylene bisimide dye. *Adv. Mater.* **24**, 3350–3355 (2012).

35. J. Mizuguchi, Electronic characterization of N,N[sup ']-bis(2-phenylethyl)perylene-3,4: 9, 10-bis(dicarboximide) and its application to optical disks. *J. Appl. Phys.* **84**, 4479 (1998).

36. M. Dharmarwardana *et al*., Thermo-mechanically responsive crystalline organic cantilever. *Chem. Commun.* **53**, 9890–9893 (2017).

37. M. Dharmarwardana *et al*., Rapidly reversible organic crystalline switch for conversion of heat into mechanical energy. *J. Am. Chem. Soc.* **143**, 5951–5957 (2021).

38. M. Dharmarwardana *et al*., The thermo-responsive behavior in molecular crystals of naphthalene diimides and their 3D printed thermochromic composites. *CrystEngComm* **20**, 6054–6060 (2018).

39. W. Zhou, H. Wu, T. Yildirim, J. R. Simpson, A. R. H. Walker, Origin of the exceptional negative thermal expansion in metal-organic framework-5 Zn$_4$O (1,4– benzenedicarboxylate)3. *Phys. Rev. B* **78**, 054114 (2008).

40. D. R. Sears, H. P. Klug, Density and expansivity of solid xenon. *J. Chem. Phys.* **37**, 3002 (1962).

41. A. Warshel, E. Huler, Theoretical evaluation of potential surfaces, equilibrium geometries and vibronic transition intensities of excimers: The pyrene crystal excimer. *Chem. Phys.* **6**, 463–468 (1974).

42. H. Karabıyık, H. Karabıyık, N. Ocak İskeleli, Hydrogen-bridged chelate ring-assisted π-stacking interactions. *Acta Crystallogr. B* **68**, 71–79 (2012).

43. F. Würthner, Perylene bisimide dyes as versatile building blocks for functional supramolecular architectures. *Chem. Commun.* **21**, 1564–1579 (2004).

44. H. Naito, Y. Morisaki, Y. Chujo, o-Carborane-based anthracene: A variety of emission behaviors. *Angew. Chem. Int. Ed. Engl.* **54**, 5084–5087 (2015).

45. R. N. McDougald Jr *et al*., Molecular and electronic structure of cyclic trinuclear gold(I) carbeniate complexes: Insights for structure/luminescence/conductivity relationships. *Inorg. Chem.* **53**, 7485–7499 (2014).

46. F. Graser, E. Hädike, Kristallstruktur und Farbe bei Perylen-3,4;9,10-bis(dicarboximid)-Pigmenten,2. *Liebigs Ann. Chem.* **1984**, 483–494 (1984).

47. M. A. Rawashdeh-Omary, M. A. Omary, H. H. Patterson, Oligomerization of Au(C-N)$_2^-$and Ag(CN)$_2^-$ ions in solution via ground-state aurophilic and argentophilic bonding. *J. Am. Chem. Soc.* **122**, 10371–10380 (2000).

48. J. W. Schindler, R. C. Fukuda, A. W. Adamson, Photophysics of aqueous tetracyanoplatinate(2-). *J. Am. Chem. Soc.* **104**, 3596–3600 (1982).

49. F. M. Winnik, Photophysics of preassociated pyrenes in aqueous polymer solutions and in other organized media. *Chem. Rev.* **93**, 587–614 (1993).

50. A. K.-W. Chan, V. W.-W. Yam, Precise modulation of molecular building blocks from tweezers to rectangles for recognition and stimuli-responsive processes. *Acc. Chem. Res.* **51**, 3041–3051 (2018).

51. Y. Li, K. M.-C. Wong, A. Y.-Y. Tam, L. Wu, V. W.-W. Yam, Thermo- and acid-responsive photochromic spironaphthoxazine-containing organogelators. *Chemistry* **16**, 8690–8698 (2010).

52. S. Grimme, Do special noncovalent π-π stacking interactions really exist? *Angew. Chem. Int. Ed. Engl.* **47**, 3430–3434 (2008).

53. N. J. Turro, *Modern Molecular Photochemistry* (University Science Books, 1991).

54. S. Grimme, Seemingly simple stereoelectronic effects in alkane isomers and the implications for Kohn-Sham density functional theory. *Angew. Chem. Int. Ed. Engl.* **45**, 4460–4464 (2006).

55. Y. Zhao, D. G. Truhlar, A density functional that accounts for medium-range correlation energies in organic chemistry. *Org. Lett.* **8**, 5753–5755 (2006).

56. A. K. Bauer *et al*., Environmentally prevalent polycyclic aromatic hydrocarbons can elicit co-carcinogenic properties in an in vitro murine lung epithelial cell model. *Arch. Toxicol.* **92**, 1311–1322 (2018).

57. M. Nakamura *et al*., Pyrene is highly emissive when attached to the RNA duplex but not to the DNA duplex: The structural basis of this difference. *Nucleic Acids Res.* **33**, 5887–5895 (2005).

58. B. Dunn, J. I. Zink, Molecules in glass: Probes, ordered assemblies, and functional materials. *Acc. Chem. Res.* **40**, 747–755 (2007).

59. O. M. El-Kadri *et al*., Pyrene bearing azo-functionalized porous nanofibers for CO$_2$ separation and toxic metal cation sensing. *ACS Omega* **3**, 15510–15518 (2018).

60. M. K. Panda *et al*., Strong and anomalous thermal expansion precedes the thermosalient effect in dynamic molecular crystals. *Sci. Rep.* **6**, 29610 (2016).

61. A. S. Sergeenko, J. S. Ovens, D. B. Leznoff, Designing anisotropic cyanometallate coordination polymers with unidirectional thermal expansion (TE): 2D zero and 1D colossal positive TE. *Chem. Commun.* **54**, 1599–1602 (2018).